Estimating stellar population and emission-line properties in S-PLUS galaxies

J. Thainá-Batista [1]⋆ R. Cid Fernandes [1], F. R. Herpich [2,3] C. Mendes de Oliveira,[2] A. Werle [4], L. Espinosa,[2] A. Lopes,[5] A. V. Smith Castelli,[5,6] L. Sodré [2], E. Telles,[7] A. Kanaan,[1] T. Ribeiro[8] and W. Schoenell[9]

[1]*Departamento de Física – CFM – Universidade Federal de Santa Catarina, PO Box 476, 88040-900 Florianópolis, SC, Brazil*
[2]*Departamento de Astronomia, Instituto de Astronomia, Geofísica e Ciências Atmosféricas da USP, Cidade Universitária, 05508-900 São Paulo, SP, Brazil*
[3]*Cambridge Astronomy Survey Unit, Institute of Astronomy, Madingley Road, Cambridge CB3 0HA, UK*
[4]*INAF – Osservatorio Astronomico di Padova, Vicolo dell'Osservatorio 5, I-35122 Padova, Italy*
[5]*Instituto de Astrofsica de La Plata, CONICET–UNLP, Paseo del Bosque s/n, B1900FWA La Plata, Argentina*
[6]*Facultad de Ciencias Astronómicas y Geofísicas, Universidad Nacional de La Plata, Paseo del Bosque s/n, B1900FWA La Plata, Argentina*
[7]*Observatório Nacional, Rua General José Cristino 77, CEP 20921-400 São Cristóvão, Rio de Janeiro, Brazil*
[8]*NOAO, 950 North Cherry Avenue, Tucson, AZ 85719, USA*
[9]*GMTO Corporation, North Halstead Street 465, Suite 250, Pasadena, CA 91107, USA*

ABSTRACT

We present tests of a new method to simultaneously estimate stellar population and emission-line (EL) properties of galaxies out of the Southern Photometric Local Universe Survey (S-PLUS) photometry. The technique uses the ALSTAR code, updated with an empirical prior that greatly improves its ability to estimate ELs using only the survey's 12 bands. The tests compare the output of (noise-perturbed) synthetic photometry of the Sloan Digital Sky Survey (SDSS) galaxies to properties derived from previous full spectral fitting and detailed EL analysis. For realistic signal-to-noise ratios, stellar population properties are recovered to better than 0.2 dex in masses, mean ages, metallicities, and ±0.2 mag for the extinction. More importantly, ELs are recovered remarkably well for a photometric survey. We obtain input − output dispersions of 0.05–0.2 dex for the equivalent widths of [O II], [O III], Hβ, Hα, [N II], and [S II], and even better for lines stronger than ∼5 Å. These excellent results are achieved by combining two empirical facts into a prior that restricts the EL space available for the fits. (1) Because, for the redshifts explored here, Hα and [N II] fall in a single narrow band (J0660), their combined equivalent width is always well recovered, even when [N II]/Hα is not. (2) We know from SDSS that $W_{H\alpha+[N II]}$ correlates with [N II]/Hα, which can be used to tell if a galaxy belongs to the left or right wings in the classical Baldwin–Phillips–Telervich (BPT) diagnostic diagram. Example applications to integrated light and spatially resolved data are also presented, including a comparison with independent results obtained with the Multi-Unit Spectroscopic Explorer (MUSE)-based integral field spectroscopy.

Key words: methods: data analysis – techniques: photometric – astronomical data bases: miscellaneous – galaxies: general – galaxies: stellar content.

1 INTRODUCTION

The Southern Photometric Local Universe Survey (S-PLUS) is an ongoing project based on an 80-cm robotic telescope located at Cerro Tololo (Chile), which gathers images on five broad and seven narrow bands spanning the ∼3500–9000 Å range. Like its northern twin, the Javalambre Photometric Local Universe Survey (J-PLUS; Cenarro et al. 2019), the S-PLUS is a multipurpose survey, with applications ranging from Solar system to extragalactic scales. A full description of S-PLUS is given in Mendes de Oliveira et al. (2019). Some of its first results are reported in Barbosa et al. (2020), Molino et al. (2020), Lima-Dias et al. (2021), Whitten et al. (2021), Placco et al. (2021), Nakazono et al. (2021), Lima et al. (2022), and Almeida-Fernandes et al. (2022).

This paper addresses the question of how to use S-PLUS data to characterize the basic stellar population and emission-line (EL) properties of galaxies. Estimates of properties like stellar masses, mean stellar ages, and emission line equivalent widths are to study a variety of science cases in galaxy evolution, like those involving galaxy morphology or environment, as well as in the spatially resolved analysis of nearby galaxies. The literature is plentiful on methods and tools to fit the spectral energy distribution (SED) of galaxies, both for spectroscopic and photometric data (see Conroy 2013; Carnall et al. 2019; Leja et al. 2019). Few, however, have been tested with the S-PLUS filter system, whose peculiar combination of narrow and broad bands calls for simultaneous analysis of stellar and nebular emission components. Vilella-Rojo et al. (2015) and Logroño-García et al. (2019) did explore this issue in the context of J-PLUS, but focusing on the estimation of the Hα fluxes, while Lumbreras-Calle et al. (2022) did so mainly for the [O III] line in galaxies with extremely intense emission.

⋆ E-mail: jullia.thainna@gmail.com

We present a series of experiments with the ALSTAR code, applied to both simulated and actual S-PLUS data. ALSTAR was first presented in González Delgado et al. (2021, hereafter GD21) in a study of galaxies in the mini Javalambre Physics of the Accelerating Universe Astrophysical Survey (miniJPAS; Bonoli et al. 2021). Besides the very different number of bands (12 versus 56), in GD21, all bands potentially contaminated by [O II]3726, 3729, Hβ, [O III]4959, 5007, Hα, and [N II]6548, 6584 were discarded from the analysis, whereas here we do not perform such masking. Instead, we simultaneously model both stellar and nebular emissions using a semi-empirical approach that ensures that the resulting ELs are realistic.

The paper is organized as follows. Section 2 describes the ALSTAR code. Emphasis is given to how we account for ELs, as this is the most innovative aspect of this study. Section 3 presents a series of simulations to evaluate the ability of the code to retrieve stellar and nebular properties out of S-PLUS photometry under different noise levels. The input in these simulations is based on the Sloan Digital Sky Survey (SDSS) spectra whose stellar populations and ELs have been previously analysed by Werle et al. (2019, hereafter W19) with the STARLIGHT (Cid Fernandes et al. 2005) and DOBBY codes (Vale Asari et al. 2019). Section 4 presents a few example applications to actual S-PLUS data, including the analysis of a data cube of a nearby spiral galaxy. Finally, Section 5 summarizes our main results.

2 SPECTRAL SYNTHESIS

The analysis of galaxy SEDs employing fits with stellar population models dates back to Tinsley and others in the 1970s (see Walcher et al. 2011; Conroy 2013 for reviews). This spectral synthesis approach, as it is sometimes called, has progressed substantially in the last two decades with extensive work on evolutionary tracks and libraries of stellar spectra, resulting in improved models for stellar populations of different ages and metallicities. These key ingredients are used in codes that mix these populations (following either parametric or non-parametric prescriptions) to estimate properties such as stellar masses, mean stellar ages and metallicities, and dust content by comparing the models to spectroscopic (e.g. Asari et al. 2007; Riffel et al. 2009) or photometric data (e.g. da Cunha, Charlot & Elbaz 2008; Noll et al. 2009; Chevallard & Charlot 2016; Carnall et al. 2018).

The ALSTAR code described in this section performs a non-parametric decomposition of the input photometric (and spectroscopic, when available) fluxes in terms of a spectral base composed of stellar populations and, optionally, ELs. The code was introduced and compared with three other codes in GD21 in an analysis of ~8500 galaxies in the All-Wavelength Extended Groth Strip International Survey (AEGIS) field (the miniJPAS survey; Bonoli et al. 2021). The data comprised photometry covering the ~3500–9300 Å range obtained with 54 narrow-band filters [full width at half-maximum (FWHM) ~ 145 Å] spaced by ~100 Å, plus two broader bands at the blue and red ends. The analysis focused entirely on the stellar population properties retrieved by the different codes. The potential effects of nebular emission on the photometry were circumvented by removing all bands covering the main optical ELs from the fits. The performance of ALSTAR in dealing with ELs was therefore *not* tested in GD21.

While suitable for spectroscopy (or when tens of narrow bands are available), the strategy of (i) masking ELs, (ii) fitting the stellar continuum on the unmasked data, and (iii) measuring ELs from the residual spectrum is clearly not an optimal workflow in the case of S-PLUS. First, ELs are present in all bands, so neglecting

their effect in some filters (say, the broad-bands) already limits the precision of the stellar continuum fits. Secondly, the amount of EL information retrievable from such a residual photospectrum would be very limited, with no guarantee that the inferred line fluxes are realistic.

This paper showcases our method to account simultaneously for stellar and nebular emission in ALSTAR. The method applies to any set of filters, but we focus on the 12 S-PLUS bands. We start by summarizing the base of stellar population models employed and how dust attenuation is modelled (Section 2.1). We then present our semi-empirical approach to account for ELs (Section 2.2), and how we tune it to improve the results (Section 2.3).

2.1 Stellar population base and dust attenuation

The main stellar population base used in this work is the same as in GD21 and very similar to the one in W19. Briefly, it contains spectra for 16 logarithmically spaced age bins spanning from $t = 1$ Myr to 14 Gyr, and seven metallicities from $Z = 0.005$ to 3.5 $Z_\odot$, built out of an updated version of the Bruzual & Charlot (2003) models (see Vidal-García et al. 2017; W19 for details on the evolutionary tracks and spectral libraries involved). A Chabrier (2003) initial mass function is adopted.

Dust attenuation is parametrized by the V-band optical depth (τ) and is modelled with a Calzetti et al. (2000) law in all cases in this paper. ALSTAR allows for up to two different values of τ: one applied to the full base (τ_{ISM}) and an extra one (τ_{BC}) to just some components. The motivation is to allow young stars to suffer an extra attenuation due to dust in their surrounding birth clouds (the so-called differential-extinction phenomenon; Calzetti, Kinney & Storchi-Bergmann 1994; Charlot & Fall 2000). The two τs can be either free or tied together. We chose to set $\tau_{BC} = 1.27\tau_{ISM}$ for ≤10 Myr stars (as well as ELs) so that these components are 2.27 times as attenuated as older populations (cf. Calzetti 2001). Other configurations are possible, including some where τ_{BC} is not necessarily associated with birth clouds, but these will not be explored in this work.

After fitting the photometry, ALSTAR outputs how much each base component contributes to the flux at a chosen reference rest-frame wavelength of 5635 Å, from which other properties like stellar masses and (light or mass weighted) mean ages can be readily computed. To put it in mathematical terms, the model for the stellar spectrum reads

$$M_\lambda^\star = \sum_{j=1}^{n_\star} x_j b_{\lambda,j}^\star \, e^{-\tau_j q_\lambda}, \tag{1}$$

where $b_{\lambda,j}^\star$ is the spectrum of population j (age t_j and metallicity Z_j) scaled to 1 at $\lambda = 5635$ Å, $q_\lambda = \tau_\lambda/\tau_V$ is the reddening law, and $\tau_j = \tau_{ISM}$ for $t_j > 10$ Myr or $\tau_j = \tau_{ISM} + \tau_{BC} = 2.27\tau_{ISM}$ for younger populations. The parameters in this model are the x_j fluxes of the $n_\star$ populations and τ_{ISM}, while $b_{\lambda,j}^\star$ and q_λ are its ingredients.

The fit is repeated $n_{MC} = 100$ times perturbing the input fluxes with the corresponding errors. These Monte Carlo (MC) runs map both noise-induced uncertainties and the degeneracies inherent to spectral synthesis.

2.2 The emission-line base

ELs are accounted for with a novel approach that incorporates them in the spectral base in a constrained manner. Five sets of lines are considered: the [O II]λλ3726, 3729 doublet, [O III]λλ4959,
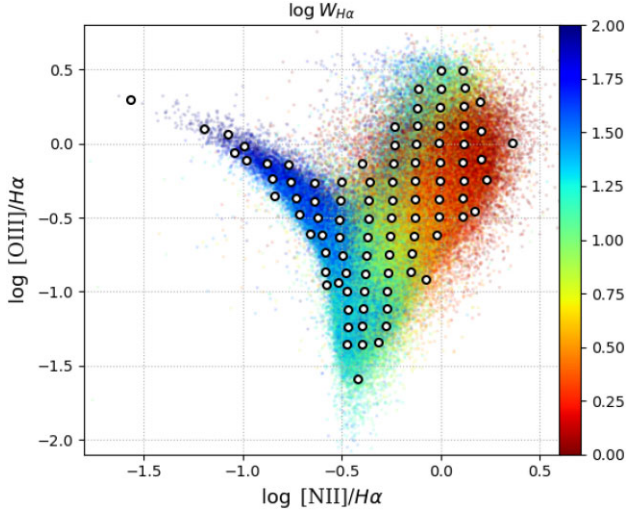
Figure 1. The BPTα diagram for SDSS galaxies (dots, coloured by log $W_{H\alpha}$ [Å]) and our EL base component (white circles). All line fluxes are dereddened, but this is only relevant for the *y*-axis, which differs from the usual log[O III]/Hβ by ∼−0.5 dex.

5007, [N II]λλ6548, 6584, [S II]λλ6717, 6731, and the Balmer series (from Hα to Hε).[1] Each of these sets has relative line intensity ratios pre-defined by nebular physics. The [O III]5007/[O III]4959 and [N II]6584/[N II]6548 flux ratios are fixed at 3, while the relative strengths of the [S II] lines are fixed at its [S II]6717/[S II]6731 = 1.4 low-density limit, and similarly for [O II]3726/[O II]3729. The relative strengths of Balmer lines are fixed at the values obtained for an H II region with electron temperature 10^4 K and density 10^2 cm^{-3}, as given in the emissivity tables of Dopita & Sutherland (2003).

We impose that all ELs must be present simultaneously, and in proportions found in real galaxies. The way this idea is implemented is illustrated in Fig. 1, which shows the Baldwin–Phillips–Televich α (BPTα) diagram, a trivial variation over the original Baldwin, Phillips & Terlevich (1981) diagram, where instead of [O III]/Hβ the *y*-axis shows the dereddened [O III]/Hα flux ratio, a physically irrelevant choice that is convenient here because we define our EL base to have unit flux in Hα. The dots come from a sample of over 200 000 SDSS galaxies analysed in Cid Fernandes et al. (2010), coloured by the Hα equivalent width ($W_{H\alpha}$). White circles show the loci of the n_{EL} = 94 components in our EL base. Their coordinates are defined as the mean log line ratios in a grid of 0.125 dex square bins containing at least 200 galaxies, plus a few extra points added to better trace the outer contours of the observed distribution. The values of [O II]/Hα and [S II]/Hα for each component were also defined as the average in each BPTα bin.

The spectrum of each EL base component is built to have unitary Hα flux, Gaussian profiles with $\sigma = 150$ km s^{-1}, and dust-free line ratios defined as explained above. Nebular continuum emission is neglected. Fig. 2 shows a couple of example spectra, along with the corresponding S-PLUS photometry from u_{JAVA} ($\lambda_{pivot} = 3533$ Å) to J0660 ($\lambda_{pivot} = 6614$ Å). The spectra are shifted to redshift $z = 0.01$, such that the main ELs fall within narrow bands, and (for this very reason) typical of the main intended applications. As expected,

---

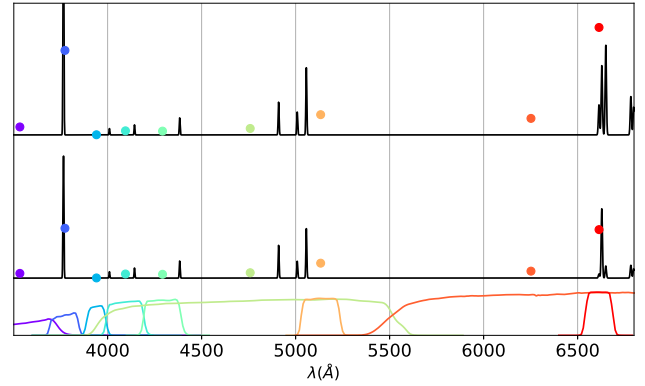**Figure 2.** Example EL base spectra corresponding to a typical SF galaxy (bottom) and a retired galaxy (top) – located at (log[N II]/Hα, log[O III]/Hα) = (−0.76, −0.26) and (0.11, −0.13), respectively. Both are redshifted to $z = 0.01$. The coloured points show the corresponding S-PLUS photometric fluxes, multiplied by 10 for clarity. The bottom curves show the S-PLUS filter transmission profiles in the range from u_{JAVA} to J0660.

ELs stand out clearly in the narrow bands. The final effect on the photometry, of course, depends on the stellar continuum to which the lines are added. The contribution of an EL of equivalent width W to a filter of width Δ is $\approx W/(W + \Delta)$. For a star-forming (SF) galaxy like the bottom one in Fig. 2, the EL contribution to J0660 (*r*) exceeds 50 (9) per cent for $W_{H\alpha} > 119$ Å.

The top EL spectrum in Fig. 2 is typical of that of a retired galaxy, i.e. a galaxy with no ongoing star formation nor relevant nuclear activity, and whose EL are powered only by hot, low-mass evolved stars (Stasińska et al. 2008). These systems have typically $W_{H\alpha}$ of ∼1 Å (Cid Fernandes et al. 2011), in which case (and further assuming [N II]/Hα ∼ 1.3) the EL contribution to the J0660 flux would be just ∼2 per cent, and negligible to the *r* band.

By construction, the linear combinations of these components computed by ALSTAR approximately span the space of line ratios observed in real galaxies. The output in this case is the contribution of each component to the Hα flux, to which all other lines are scaled. Mathematically, the EL model spectrum reads

$$M_\lambda^{EL} = \sum_{j=n_\star+1}^{n_\star+n_{EL}} x_j b_{\lambda,j}^{EL} \, e^{-\tau_j q_\lambda}, \tag{2}$$

where $b_{\lambda,j}^{EL}$ is the EL spectrum normalized to unitary $F_{H\alpha}$ (such as those exemplified in Fig. 2) and x_j is the Hα flux in component *j*. The total model combines the stellar (equation 1) and EL (equation 2) components: $M_\lambda = M_\lambda^\star + M_\lambda^{EL}$.

As with the stellar components, ELs are attenuated by either $\tau_{ISM}(\lambda)$ or $\tau_{ISM}(\lambda) + \tau_{BC}(\lambda)$, depending on the configuration. In this study, we chose to link the attenuation of the EL base components to that of young stars, which is itself tied to that of the general interstellar medium (ISM).

The fact that both ELs and ≤10 Myr stars undergo the same dust attenuation is the only link between stellar populations and ELs imposed in our fits. The model can be easily modified to impose some level of consistency between these two types of components. For instance, instead of treating it as a free parameter, the Hα flux can be computed in terms of the ionizing photon flux produced by the same stars used to model the continuum, effectively linking stellar populations and ELs in an astrophysical way (as done, for instance, in Carnall et al. 2018). Note, however, that even this simple
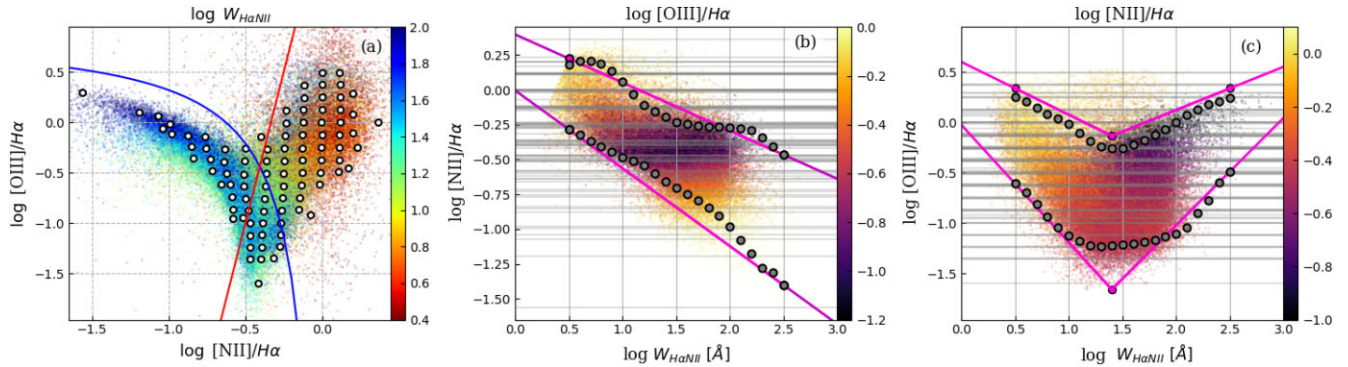
---

[1] We denote [O II]λλ3726 + 3729, [O III]λ5007, [N II]λ6584, and [S II]λλ6716 + 6731 by [O II], [O III], [N II], and [S II], respectively. The combination of Hα with both the [N II]λλ6548, 6584 lines is denoted by Hα N II.

Figure 3. (a) As Fig. 1, but colouring by the log of $W_{\mathrm{H}\alpha\,\mathrm{N\,II}} = W_{\mathrm{H}\alpha} + W_{[\mathrm{N\,II}]6548} + W_{[\mathrm{N\,II}]6584}$. The blue and red curves are part of the EL base restriction scheme discussed in the text (see Table 1). (b) log[N II]/Hα versus $W_{\mathrm{H}\alpha\,\mathrm{N\,II}}$, coloured by log[O III]/Hβ. (c) Like panel (b), but for [O III]/Hβ, and colour coding by log[N II]/Hα. Dark circles in panels (b) and (c) track the 5 and 95 percentile curves, while horizontal grey lines mark the log line ratios in the full EL base. The magenta lines show the lower and upper limits imposed to limit the EL base for a given $W_{\mathrm{H}\alpha\,\mathrm{N\,II}}$. These limits refine the left/right wing constraints shown in panel (a). Together, they work as a prior that helps estimating EL properties out of the always reliable estimate of $W_{\mathrm{H}\alpha\,\mathrm{N\,II}}$.

refinement requires full confidence on the model stellar spectra in the <912 Å range, as well as a recipe to deal with the dust extinction of these ionizing photons, and an assumption about their escape fraction. Given the uncertainties in all these factors, we opted not to incorporate them in this first study.

2.2.1 Single emission-line base components do not work

Before moving on, let us open a parenthesis to dismiss the naive idea that a compact EL base containing just one of the main ELs per component (and zero flux in the other lines) would be preferable to the scheme outlined above.

Besides allowing for arbitrary line ratios, this smaller base would (somewhat counter-intuitively) give much more freedom to the code. Too much freedom, in fact. Consider, for instance, the case of a galaxy with no ELs at all (or very weak ones), but where the filter containing, say, [O III], has a positive noise spike that prevents it from being fitted by the stellar base alone. The code could then simply attribute this extra flux to a non-existent [O III] and fit the observed flux exactly, even if no other EL is found or if it implies [O III]/Hβ > 1000.

This deceivingly simpler base can thus lead to non-physical line ratios and be misused to fit (positive) noise or compensate for deficiencies in the stellar base. This was verified in numerical experiments, which also showed that even when ELs are strong the fits often lead to unrealistic line ratios.

2.3 Equivalent-width-based constraints

The approach of tying all ELs together and constraining them to realistic proportions should provide a reasonable estimate of their effect on the S-PLUS photometry (not only the narrow bands) and hence aid the ALSTAR fits. One should not, however, expect the ELs to be reliably retrieved, as there is not enough information in the 12 S-PLUS bands to properly constrain them in detail.

The main problem is that Hα and the adjacent [N II] lines all fall into a single filter, J0660, centred at 6614 Å and with a FWHM of 147 Å (Mendes de Oliveira et al. 2019). The code should be able to handle well the combined effect of Hα + [N II] on the J0660 filter (as shown by Vilella-Rojo et al. 2015), but disentangling them is a harder task. Tests confirmed that while ALSTAR recovers the combined [N II]6548 + Hα + [N II]6584 equivalent width (hereafter

$W_{\mathrm{H}\alpha\,\mathrm{N\,II}}$) very accurately, the [N II]/Hα ratio can come out completely wrong, moving a galaxy from left to right or vice versa in the BPT diagram. Other lines, besides being generally weaker, do not have the ability to distinguish which wing of the BPT 'seagull' a galaxy sits in, seriously limiting the kind of EL-based diagnostic doable with S-PLUS.

A possible strategy to deal with this limitation is to restrict the EL base to just one of the wings, chosen on the basis of ancillary data (say, X-rays). Some sort of base restriction is in order, but this is not a satisfactory general solution. Our challenge here is to mitigate this problem using only S-PLUS data.

We have developed a semi-empirical method to tackle this issue. The key idea is to explore the fact that EL equivalent widths are generally larger in SF than in the so-called active galactic nucleus (AGN) wing.[2] This is clearly seen in Fig. 1. The SF wing is composed almost exclusively by galaxies with $W_{\mathrm{H}\alpha} \gtrsim 50$ Å (painted in green–blue), increasing to over 100 Å towards the top-left. Right wing sources have generally lower $W_{\mathrm{H}\alpha}$, including the whole population of retired galaxies (in red) with $W_{\mathrm{H}\alpha}$ of order 1 Å. Some Seyfert 2s (towards the top-right) have Hα in the range of SF galaxies, but otherwise $W_{\mathrm{H}\alpha}$ offers a good way of distinguishing left from right wing sources.

As discussed above (and demonstrated in Section 3.4), we cannot trust our initial estimates of $W_{\mathrm{H}\alpha}$, but $W_{\mathrm{H}\alpha\,\mathrm{N\,II}} \equiv W_{\mathrm{H}\alpha} + W_{[\mathrm{N\,II}]6548} + W_{[\mathrm{N\,II}]6584}$ is very reliable. We thus seek a scheme based on this robust quantity to restrict the EL base. Fig. 3(a) repeats Fig. 1, this time colouring galaxies by $W_{\mathrm{H}\alpha\,\mathrm{N\,II}}$. The general appearance of the two plots is the same. Visibly, knowledge of the value of $W_{\mathrm{H}\alpha\,\mathrm{N\,II}}$ provides valuable guidance on the whereabouts of a galaxy in the BPT diagram.

After some experimentation, we have adopted the following scheme to incorporate this prior knowledge in our analysis.

(i) We run an initial fit with the full EL base to estimate $W_{\mathrm{H}\alpha\,\mathrm{N\,II}}$ (this initial value is robust even when [N II]/Hα comes out wrong.

---

[2]Despite its common use in the literature, 'AGN wing' is a misnomer, given that the right wing in the BPT diagram also contains large proportions of galaxies where both AGN and SF activity coexist, as well as plenty of retired galaxies, which have neither ongoing SF nor an energetically relevant AGN (Stasińska et al. 2008; Cid Fernandes et al. 2011).

Table 1. Equations used to constrain the EL base according to the value of $W_{\mathrm{H\alpha\,N\,II}}$ – see also Fig. 3.

Constraint	$W_{\mathrm{H\alpha\,N\,II}}$ range
$\log[\mathrm{O\,III}]/\mathrm{H\alpha} < 0.90 + 0.61/(\log[\mathrm{N\,II}]/\mathrm{H\alpha} - 0.05)$	≥ 50 Å
$\log[\mathrm{O\,III}]/\mathrm{H\alpha} > 6\log[\mathrm{N\,II}]/\mathrm{H\alpha} + 2$	≤ 10 Å
$\log[\mathrm{N\,II}]/\mathrm{H\alpha} \leq -0.345\min(\log W_{\mathrm{H\alpha\,N\,II}}, 3) + 0.397$	Any
$\log[\mathrm{N\,II}]/\mathrm{H\alpha} \geq -0.559\max(\log W_{\mathrm{H\alpha\,N\,II}}, 0) - 0.005$	Any
$\log[\mathrm{O\,III}]/\mathrm{H\alpha} \leq -0.523\log W_{\mathrm{H\alpha\,N\,II}} + 0.598$	<25 Å
$\log[\mathrm{O\,III}]/\mathrm{H\alpha} \leq 0.428\log W_{\mathrm{H\alpha\,N\,II}} - 0.734$	≥ 25 Å
$\log[\mathrm{O\,III}]/\mathrm{H\alpha} \geq -1.164\max(\log W_{\mathrm{H\alpha\,N\,II}}, 0) - 0.026$	<25 Å
$\log[\mathrm{O\,III}]/\mathrm{H\alpha} \geq 1.063\max(\log W_{\mathrm{H\alpha\,N\,II}}, 2.85) - 3.144$	≥ 25 Å

(ii) We first limit the EL base to the left of the blue line in Fig. 3(a) when $W_{\mathrm{H\alpha\,N\,II}} > 50$ Å, and to the right of the red one when $W_{\mathrm{H\alpha\,N\,II}} < 10$ Å. Points in the $W_{\mathrm{H\alpha\,N\,II}} = 10$–50 Å region are not constrained by this first cut.

(iii) We then compute lower and upper limits for [N II]/Hα as a function of $W_{\mathrm{H\alpha\,N\,II}}$. This was done essentially in a visual way examining Fig. 3(b).

(iv) The very shape of the wings in the BPT diagram implies that limits in its *x*-axis translate onto the *y*-axis. We reinforce this implicit constraint by imposing limits on [O III]/Hα as a function of $W_{\mathrm{H\alpha\,N\,II}}$ (Fig. 3c).

The equations involved in this heuristic scheme are given in Table 1. Only base components satisfying these $W_{\mathrm{H\alpha\,N\,II}}$-based constraints are allowed for in the fits. The most notable 'victims' of this scheme are Seyfert 2s, some of which are legitimate right wing sources with $W_{\mathrm{H\alpha\,N\,II}} > 50$ Å that are forced to move to the left wing by step (ii) above. More refined schemes may be able to deal with this caveat, but we chose to overlook it in this paper.[3]

Finally, we note that while the specific criteria delineated here were based on integrated galaxy data from the SDSS, spatially resolved studies can straightforwardly adjust them to better represent spaxel-based ELs, obtained from surveys like Calar Alto Legacy Integral Field Area (CALIFA; Sánchez et al. 2016) or Mapping Nearby Galaxies at Apache Point Observatory (MaNGA; Bundy et al. 2015). Previous EL work on these surveys, however, suggests that our criteria would remain approximately the same for spatially resolved data (see, for instance, fig. 25 in Sánchez et al. 2022).

The effective role of these criteria is to incorporate prior information on the properties of ELs in actual galaxies, hopefully aiding a more accurate retrieval of their properties out of the data offered by S-PLUS. The aim is obviously not to reach a spectroscopy-quality quantification of EL properties, but to mimic it as best as possible. Several refinements and extensions of this general idea can be explored, but we leave this for future work. Let us now put this scheme to test, first with a suite of simulations (Section 3) and then with some example applications to actual data (Section 4).

3 SIMULATIONS

In order to test ALSTAR in the S-PLUS regime we have culled a sample of SDSS galaxies previously analysed by means of full

---

[3]If additional e.g. X-rays suggest that the galaxy has an AGN, then one may trivially adjust the EL base to focus on AGN-like components. In such cases one may further add AGN-like (say, power law) components to the stellar population base to account for the non-stellar continuum emission of AGN, as done in the spectroscopic studies (e.g. Cid Fernandes et al. 2004).

spectral synthesis and detailed EL fitting as a reference. We have selected 10 473 SDSS galaxies out of those analysed by W19 with the STARLIGHT and DOBBY codes for this experiment. The test consists of computing the synthetic photometry of these galaxies, adding noise, running it through ALSTAR, and comparing its output with that obtained by W19.

3.1 The input

Our sample was chosen to be uniformly distributed in $\log W_{\mathrm{H\alpha}}$, with 500 galaxies randomly drawn every 0.1 dex for $W_{\mathrm{H\alpha}}$ between 1 and 100 Å, plus 473 galaxies above 100 Å. It thus spans from retired galaxies, with their very weak ELs, to galaxies at the tip of the SF wing in the BPT diagram, where the high specific star formation rates and low gas phase metallicities lead to Hα and [O III] in excess of 100 Å. The choice to uniformly cover such a wide dynamic range is motivated by our desire to map the effect of the overall relevance of ELs, something that is suitably quantified by $W_{\mathrm{H\alpha}}$. Uncertainties and biases in the output ELs should increase as they become weaker (a trivial expectation that will soon be confirmed), and this sample selection scheme allows to track this effect cleanly.

Because the SDSS spectra do not fully cover the bluest and reddest S-PLUS filters, the synthetic photometry is carried out over the models fitted by W19 (including the DOBBY-based ELs), which do cover the full range. Also, since our analysis does not incorporate the *Galaxy Evolution Explorer* (*GALEX*) fluxes, we compare our results to those obtained in the SDSS-only fits described in W19. All spectra are shifted to $z = 0.01$ to ensure that Hα and [N II] are both within the J0660 filter.

Finally, we note that the stellar base used by W19 is very similar to the one used here, differing only in the exact definitions of age bins. The STARLIGHT fits in that study did not account for differential extinction, however, while our ALSTAR fits do. We have verified that this does not introduce any significant change in the conclusions of this paper. The main difference, of course, is that in W19 the ELs are masked from the spectral fits and measured a posteriori from the observed minus model residual spectra, while in our analysis stellar populations and ELs are estimated simultaneously.

3.2 Noise

One final ingredient we need to discuss is how noise is dealt with. We parametrize the noise amplitude by the signal-to-noise ratio in the *r*-band (S/N$_r$). Errors in the other bands are scaled to that in the *r*-band according to $\epsilon_\lambda/\epsilon_r = 3.37, 4.77, 7.44, 6.41, 5.70, 1.54, 3.27, 1.03, 0.99, 1.80$, and 1.33 for the u_{JAVA}, J0378, J0395, J0410, J0430, g, J0515, J0660, i, J0861, and z bands, respectively. This error spectrum is derived from statistics of thousands of galaxies observed by S-PLUS, and is similar to the one obtained from spaxel-based statistics in the S-PLUS data cubes analysed so far, so we take it as representative of the survey as a whole. Note that, unsurprisingly, the blue bands are much noisier than the red ones. On average over our test sample, the five bluest bands, which contain [O II] and the age-sensitive 4000 Å break, have typical S/N 5.6 times smaller than in the *r*-band.

Three values of S/N$_r$ are used in our simulations: 25, 50, and 100. Our main intended applications are for galaxies of z low enough so that [N II]6584 is still within the J0660 filter, which corresponds to $z < 0.018$. The discussion focuses on results obtained for S/N$_r = 50$, which is a compromise between the S/N$_r$ of spatially integrated data and that attainable for spatially resolved fluxes in this redshift range.
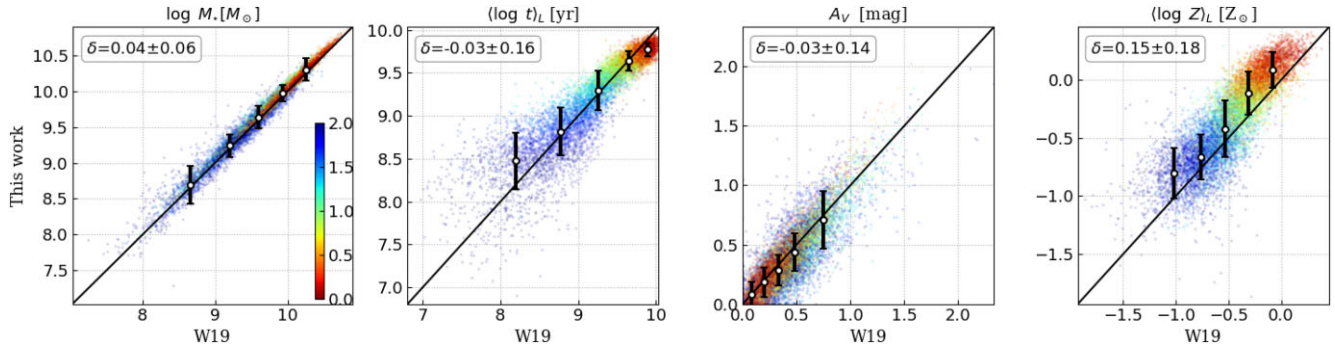
Figure 4. Comparison of the stellar population properties derived by W19 on the basis of full spectral fitting (*x*-axis) and those obtained here with S-PLUS photometry and ALSTAR (*y*-axis) for our ∼10 000 SDSS-based test sample. Points are colour coded according to the input value of log $W_{H\alpha}$ (inset colour bar in the left-hand panel). The *y*-axis represents the median values obtained in 100 MC runs for data perturbed with S/N$_r$ = 50. Error bars illustrate the typical (median σ_{NMAD}) dispersion between output and input values for bins along the *x*-axis. As in W19, the luminosity weighting in $\langle \log t \rangle_L$ and $\langle \log Z \rangle_L$ is made with the (rest-frame) flux around 5635 Å.

Each galaxy is fitted $n_{MC} = 100$ times, perturbing the input photometry with Gaussian noise with amplitude defined by ϵ_λ scaled to reach the target S/N$_r$. The intended role of these MC runs is to estimate the uncertainty in any given output property (say, the stellar mass $M_\star$). In these simulations, however, we also use them to estimate the property itself, which we do using the median value over the MC runs. The reason why this is preferable to using the best-fitting result is that the input data are built out of models that (except for the ELs) use essentially the same ingredients used in the ALSTAR fits. Despite the huge difference between the ∼4000 spectroscopic fluxes used in the original full spectral analysis and the 12 S-PLUS bands used here, it is more appropriate to report the results obtained from the analysis of the noise-perturbed runs than those resulting from fits of idealized noiseless data.

Let us now see what these simulations teach us.

3.3 Stellar population properties

Despite our particular interest in ELs, we also want to test how well the code retrieves basic stellar population properties like the stellar mass, light- and mass-weighted mean ages and metallicities, and dust content, so let us check these first.

Fig. 4 compares stellar masses ($M_\star$), luminosity-weighted mean log stellar age ($\langle \log t \rangle_L$) and metallicity ($\langle \log Z \rangle_L$), and stellar extinction (A_V) obtained by W19 with those derived here. The ALSTAR values (in the *y*-axis) are the median over the 100 MC fits for each galaxy in the S/N$_r$ = 50 runs. Points are coloured according to the input log $W_{H\alpha}$ to map the overall influence of ELs on the photometry (and hence on the ALSTAR fits). Each panel lists the sample median $\pm$ the normalized median absolute deviation (σ_{NMAD})[4] of δ, where δ denotes the output minus input difference in the corresponding property. The error bars break down the statistics of δ for bins along the *x*-axis.

The figure shows a satisfactory level of agreement, especially considering that ALSTAR used only the 12 S-PLUS bands and had the extra burden of simultaneously accounting for ELs, whereas W19 values come from full spectral fits where ELs were masked.

As expected from previous experiments of this sort (e.g. Bell et al. 2003; Cid Fernandes et al. 2005; Taylor et al. 2011), the stellar mass

is very well recovered (left-hand panel), with a difference between output and input log $M_\star$ of just $\delta = 0.04 \pm 0.06$ dex over the whole sample. The plot also shows that sources with strong ELs (blue points) are more dispersed around the one-to-one line. Quantitatively, the scatter (σ_{NMAD}) is 0.10 dex for galaxies with $W_{H\alpha} > 30$ Å, and 0.04 dex for those with weaker Hα. This difference is partly due to the effects of ELs on the fits, and partly a consequence of the fact that the star formation histories of galaxies become increasingly skewed towards younger ages as $M_\star$ decreases (the so-called 'downsizing' phenomenon – e.g. Heavens et al. 2004). This broader mixture of populations of different ages naturally induces larger uncertainties in the mass-to-light ratio, and hence on $M_\star$.

The values of $\langle \log t \rangle_L$ (the 'mean age', for short – see e.g. GD21 for its definition), agree reasonably well, with a bias of just -0.03 and a scatter of 0.16 dex. Different factors contribute to this scatter: differences in the age bins and differential-extinction set-ups used in W19 and here, the huge compression in input information (full spectrum versus 12 bands), the need to account for ELs and stellar populations simultaneously, and noise. This last factor entails a subtlety. As already noted, though the S/N in the *r* band is 50, the blue filters are much noisier. F0395 and F0410, in particular, have errors ∼7 times larger than in *r*. These two bands trace the 4000 Å break, the most powerful stellar population age indicator in the optical range (e.g. Bruzual 1983; Kauffmann et al. 2003), inevitably affecting the estimates of $\langle \log t \rangle_L$.

The third panel in Fig. 4 compares the stellar extinction A_V values of W19 to the ones found here ($A_V = \tau_{ISM} \times 2.5 \log e$). The agreement is good: $\delta A_V = -0.03 \pm 0.14$ mag. Galaxies with strong ELs tend to scatter more around the one-to-one line ($\delta A_V = -0.04 \pm 0.20$ mag for $W_{H\alpha} > 30$ Å), but even for these the differences are acceptable given the disparity in the amount of information used in the *x* and *y* axes.

The agreement in (luminosity-weighted mean log) metallicities (right-hand panel in Fig. 4) is better than anticipated for photometric data, with a scatter of just 0.18 dex. The offset of $+0.15$ dex originates from a tendency of the MC runs to produce a broad and positively skewed distribution of $\langle \log Z \rangle_L$ values. In any case, galaxy mean stellar metallicities are hard to estimate even with spectroscopy, so the level of agreement found here is more than acceptable.

The MC runs in ALSTAR provide a measure of the uncertainties in individual galaxy properties. These MC-based uncertainties are of the same order as the dispersion in output minus input δ values reported above, but with a tendency to be larger (by factors of ∼1.3–2).

---

[4]$\sigma_{NMAD}(x) = 1.4826 \times \text{median}(|x - \text{median}(x)|)$, a robust descriptor of the width of a distribution, equivalent to the standard deviation for Gaussian data.

Table 2. Statistics of the δ = output minus input for different properties and signal-to-noise ratio (S/N) in the r band. The entries list median $\pm \sigma_{\mathrm{NMAD}}$ of δ over the 10 473 galaxies in the test sample.

Property	S/N$_r$ = 25	S/N$_r$ = 50	S/N$_r$ = 100
$\log M_\star$ (M$_\odot$)	0.03 ± 0.06	0.04 ± 0.06	0.04 ± 0.05
$\langle \log t \rangle_L$ (yr)	-0.08 ± 0.18	-0.03 ± 0.16	-0.01 ± 0.15
$\langle \log t \rangle_M$ (yr)	0.07 ± 0.10	0.08 ± 0.10	0.07 ± 0.09
$\langle \log Z \rangle_L$ (Z$_\odot$)	0.26 ± 0.19	0.15 ± 0.18	0.09 ± 0.17
$\langle \log Z \rangle_M$ (Z$_\odot$)	0.31 ± 0.26	0.19 ± 0.20	0.11 ± 0.17
A_V (mag)	-0.01 ± 0.19	0.03 ± 0.14	-0.02 ± 0.11

These differences between MC and empirical (i.e. δ-based) estimates of uncertainties decrease as S/N$_r$ increases. Taking the latter as a fiducial reference, the general conclusion here is that ALSTAR tends to overestimate the uncertainties in its derived properties, but not by a great margin.

The statistics for the S/N$_r$ = 25, 50, and 100 simulations are given in Table 2. As expected, the differences increase for noisier data and vice versa. For most properties the changes in δ are small, such that results are satisfactory even for S/N$_r$ = 25. The property whose dispersion varies the most is A_V, which nearly doubles from S/N$_r$ = 100 to 25. The table also shows that mass-weighted mean ages and metallicities are less robust than luminosity-weighted ones. This happens even in full spectral fits (see table 1 of Cid Fernandes et al. 2005 for an example), and is ultimately a consequence of the highly non-linear mass–luminosity relation of stars.

From the previous work reported in GD21 we already knew that ALSTAR has a good performance in extracting stellar population properties out of J-PAS data. The results above show that it also performs well under the S-PLUS regime, and without resorting to masking ELs.

3.4 EL properties

Let us now move to the main part of this study. We start the comparison of input and output EL properties by proving that $W_{\mathrm{H\alpha N II}}$ is indeed very well recovered by ALSTAR, a premise of the whole scheme described in Section 2.3. We then investigate how reliably individual ELs are retrieved, and how key line ratios are recovered with our methodology.

3.4.1 Hα + [N II]

Fig. 5 plots the input W19 values of $W_{\mathrm{H\alpha N II}}$ against our results for the simulations with S/N$_r$ = 50. The colouring scheme traces the signal-to-noise ratio (S/N) of $W_{\mathrm{H\alpha N II}}$, as inferred from the median (the signal) and σ_{NMAD} (the noise) values over the MC runs for each galaxy.

The agreement between SDSS and S-PLUS-based measurements is excellent, extending down to $W_{\mathrm{H\alpha N II}}$ values in the retired galaxy regime ($W_{\mathrm{H\alpha N II}} \lesssim 5$ Å).[5] The statistics of the output minus input difference is $\delta \log W_{\mathrm{H\alpha N II}} = 0.01 \pm 0.02$ dex for the 10 000 galaxies. The bias and scatter increase as $W_{\mathrm{H\alpha N II}}$ decreases, but remain small (0.08 ± 0.06 dex) even when the input $W_{\mathrm{H\alpha N II}} < 5$ Å. The results are also excellent for lower S/N$_r$ (see Table 3). This confirms the expectation that, because they are all sampled in the J0660 filter (for

---

[5]Cid Fernandes et al. (2011) define retired galaxies as those with $W_{\mathrm{H\alpha}} < 3$ Å. Given that [N II]/H$\alpha \sim 1$–2 in these systems, and that the peak in their $W_{\mathrm{H\alpha}}$ distribution is at ~ 1 Å, it is reasonable to classify $W_{\mathrm{H\alpha N II}} \lesssim 5$–6 Å systems as retired.
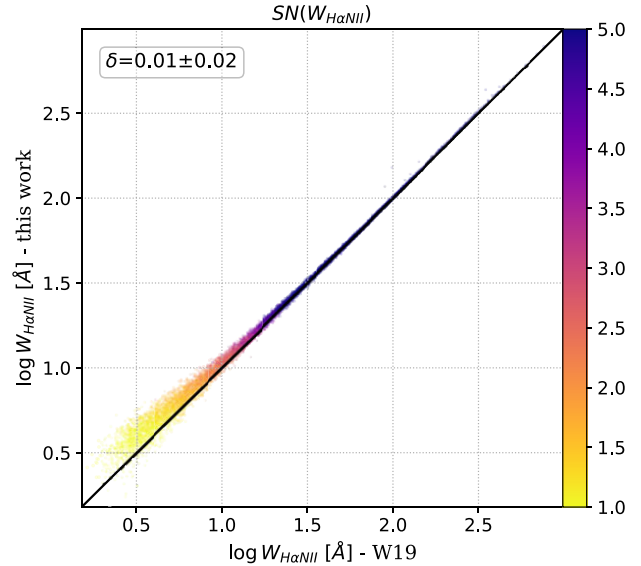
Figure 5. Comparison of the input (SDSS + STARLIGHT + DOBBY) and output (S-PLUS + ALSTAR) values of $W_{\mathrm{H\alpha N II}}$ (the combined equivalent width of Hα and [N II]6548, 6584) for the S/N$_r$ = 50 simulations. Points are coloured by the ALSTAR-based estimate of the S/N of the combined Hα and [N II]6548, 6584 equivalent widths.

the redshifts considered in this study), the combined flux of Hα and [N II] lines should be well recovered.

Careful inspection of the colours in Fig. 5 suggests that the ALSTAR MC-based S/N of $W_{\mathrm{H\alpha N II}}$ seem somewhat low for the level of agreement between input and output seen in the plot. This overestimation of the uncertainty is analogous to that identified in the examination of stellar population properties.

3.4.2 Individual lines

Fig. 6 shows how individual ELs are recovered, including Hα and [N II] separately. Unlike for [N II] + Hα, we now see substantial differences between input and output, but mainly in the bottom-left of the plots, where lines are intrinsically weak. In all cases the σ_{NMAD} of the δ = output minus input is better than 0.23 dex for the whole sample, improving to <0.15 dex when only lines stronger than 5 Å are considered (Table 3).

The best results are obtained for Hα, Hβ, and [N II] with $\sigma_{\mathrm{NMAD}} = 0.05, 0.08,$ and 0.08 dex, respectively. Despite being the second strongest EL on average in our 10 000 sample (with $\overline{W}_{[\mathrm{O II}]} = 16$ Å), [O II] is not so well recovered ($\delta = 0.04 \pm 0.16$ dex). As with the mean ages discussed above, this is due to the much larger photometric errors of the blue filters (~ 5 times larger in J0378, the filter containing [O II], than in r). The statistics barely change restricting the sample to $W_{[\mathrm{O II}]} > 5$ Å sources (Table 3), but for [O II] stronger than 10 Å the agreement improves to $\delta \log W_{[\mathrm{O II}]} = 0.02 \pm 0.09$ dex. As intuitively expected, stronger lines are better retrieved.

The worst results are found for [O III] ($\delta = 0.13 \pm 0.23$ dex), but, again, mainly when it is intrinsically weak. For galaxies where $W_{[\mathrm{O III}]} > 5$ Å we find a perfectly acceptable match: $\delta \log W_{[\mathrm{O III}]} = 0.00 \pm 0.09$ dex. Remarkably, even [S II] is well recovered, despite not falling in a narrow band, and thus having a small effect on the photometry. The reason we recover it so well is not because of its photometric relevance (typically <1 per cent of the r-band flux), but because our base ties it to other ELs in an empirically based way.

The colour scale in Fig. 6 reflects the MC-based S/N ratio of the corresponding EL. As for stellar population properties and

Table 3. Statistics of the $\delta =$ output minus input for EL properties and different S/N ratios in the *r*-band. As in Table 2, each entry gives the median $\pm \sigma_{\text{NMAD}}$ of δ for different properties (all in dex). For columns 2, 3, and 4 the statistics is performed with all 10 000 galaxies in the test sample, while in the last three columns only sources where the corresponding line is detected with $W > 5$ Å are included. For the last five rows, the >5 Å limit is applied to all ELs involved in the ratio.

| Property	All galaxies			$W \geq 5$ Å		
	S/N$_r$ = 25	50	100	25	50	100
$\log W_{\text{H}\alpha\,\text{N\,II}}$	0.03 ± 0.04	0.01 ± 0.02	0.01 ± 0.01	0.03 ± 0.03	0.01 ± 0.02	0.00 ± 0.01
$\log W_{\text{[O\,II]}}$	0.03 ± 0.19	0.04 ± 0.16	0.03 ± 0.14	0.05 ± 0.16	0.05 ± 0.15	0.03 ± 0.13
$\log W_{\text{H}\beta}$	0.04 ± 0.09	0.04 ± 0.08	0.03 ± 0.07	0.03 ± 0.04	0.02 ± 0.04	0.00 ± 0.03
$\log W_{\text{[O\,III]}}$	0.13 ± 0.26	0.13 ± 0.23	0.11 ± 0.20	0.06 ± 0.18	0.00 ± 0.09	0.00 ± 0.05
$\log W_{\text{H}\alpha}$	0.04 ± 0.06	0.01 ± 0.05	0.00 ± 0.04	0.02 ± 0.04	0.01 ± 0.03	0.00 ± 0.03
$\log W_{\text{[N\,II]}}$	0.02 ± 0.11	0.01 ± 0.08	0.01 ± 0.07	-0.03 ± 0.08	-0.01 ± 0.07	0.01 ± 0.06
$\log W_{\text{[S\,II]}}$	0.06 ± 0.14	0.03 ± 0.13	0.02 ± 0.12	0.03 ± 0.10	0.02 ± 0.09	0.01 ± 0.08
$\log[\text{N\,II}]/\text{H}\alpha$	-0.03 ± 0.13	-0.01 ± 0.12	0.00 ± 0.12	-0.05 ± 0.11	-0.02 ± 0.10	0.01 ± 0.09
$\log[\text{O\,III}]/\text{H}\beta$	0.06 ± 0.26	0.07 ± 0.23	0.05 ± 0.19	0.03 ± 0.16	0.00 ± 0.09	0.00 ± 0.06
$\log \text{H}\alpha/\text{H}\beta$	-0.01 ± 0.06	-0.02 ± 0.06	-0.03 ± 0.06	-0.02 ± 0.04	-0.01 ± 0.04	-0.01 ± 0.04
$\log[\text{O\,III}]/[\text{O\,II}]$	0.09 ± 0.23	0.07 ± 0.20	0.05 ± 0.19	0.04 ± 0.16	0.01 ± 0.09	0.01 ± 0.06
O3N2	0.09 ± 0.30	0.09 ± 0.26	0.08 ± 0.23	0.08 ± 0.26	0.00 ± 0.17	-0.02 ± 0.13
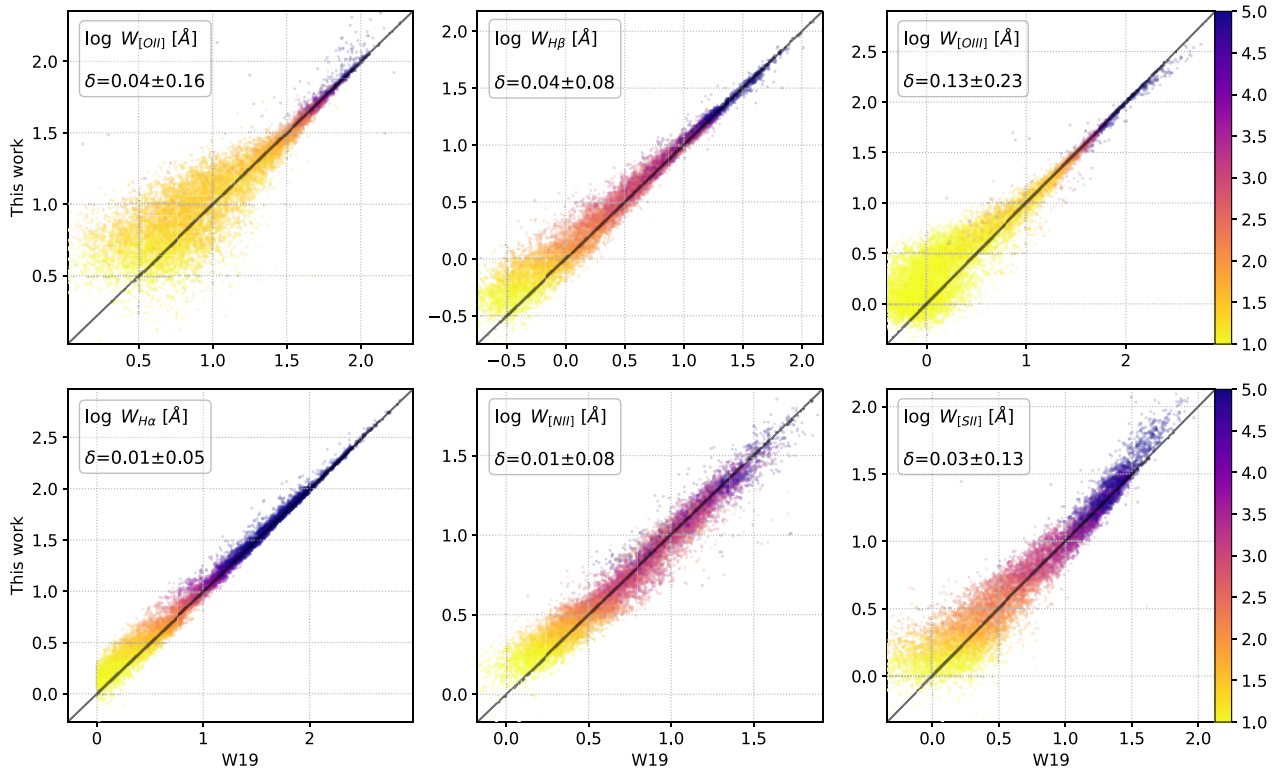
Figure 6. Comparison of input and output EL log equivalent widths for the S/N$_r$ = 50 simulations. As in Fig. 5, the colour scale reflects the median/σ_{NMAD} ratio of the corresponding line.

$W_{\text{H}\alpha\,\text{N\,II}}$, the MC uncertainties in the individual ELs are somewhat overestimated with respect to the empirical dispersion in the output versus input values.

Results for the S/N$_r$ = 25, 50, and 100 simulations are given in Table 3. The rightmost columns of the table re-evaluate the statistics of $\delta \log W$ considering only lines detected with $W > 5$ Å. The numbers confirm the visual impression from Fig. 6 that ELs above this threshold can be considered very reliable.

Inspecting Table 3 one realizes that (except for $W_{\text{[N\,II]}}$ when restricted to >5 Å) all Ws are positively biased, even if by negligible margins in most cases. This tendency to overpredict the strength of

ELs is inherent to ALSTAR. By construction, ELs can only contribute positively to the photometric fluxes, and thus may be used by the code to compensate for positive noise fluctuations if that helps improving the fit (see Section 2.2.1). Note, however, that this effect is only relevant when ELs are intrinsically weak, and thus hard to be accurately retrieved.

3.4.3 Line ratios

Finally, let us investigate some flux ratios recovered by ALSTAR. Estimating ratios is always more delicate than estimating the numer-
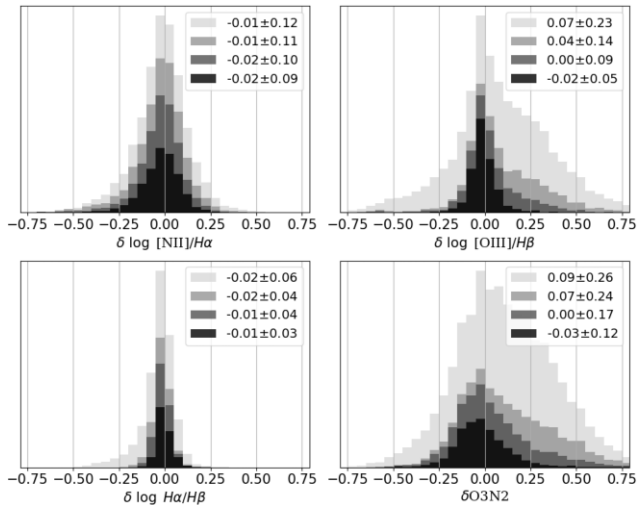
Figure 7. Histograms of the output minus input log line ratios for $S/N_r = 50$ simulations. The lighter histograms are for the 10 000 galaxies. The progressively darker ones are for subsamples defined by imposing $W > 3$, 5, and 10 Å to the lines involved in the panel. The values in the legends are the median $\pm \sigma_{\mathrm{NMAD}}$. As expected, the ratios become progressively more reliable as the lines get stronger.

ator and denominator separately, and are intrinsically biased (Rola & Pelat 1994; Wesson, Stock & Scicluna 2016). Still, because of their astrophysical relevance, it is important to test our ability to estimate line ratios out of S-PLUS data.

Fig. 7 shows histograms of the output minus input [N II]/Hα, [O III]/Hβ, and Hα/Hβ log ratios, as well as for O3N2 $= \log\{([O\,III]/H\beta)/([N\,II]/H\alpha)\}$, a popular nebular metallicity indicator (Pettini & Pagel 2004). The light shaded distributions are for the full 10 000 sample, while the darker ones are for subsamples constructed by requiring that the ALSTAR-based Ws are >3, 5, and 10 Å (light grey, dark grey, and black, respectively) for all lines involved. The statistics (median $\pm \sigma_{\mathrm{NMAD}}$) of δ are given in each panel (see also Table 3).

The figure shows that [N II]/Hα is well retrieved, with negligible bias and σ_{NMAD} decreasing from 0.12 dex for the whole sample to 0.09 dex when both [N II] and Hα have $W > 10$ Å. This success is not surprising, given the robustness of $W_{\mathrm{H}\alpha\,\mathrm{N\,II}}$ and the correlation between [N II]/Hα and $W_{\mathrm{H}\alpha\,\mathrm{N\,II}}$ on which we based our empirical EL priors. Hα/Hβ is also very well recovered, despite the fact that Hβ is only covered by a broad-band (g). This is only possible because Hβ is directly tied to Hα in our analysis.

Ratios involving [O III] are more problematic, as illustrated by the $+0.07$ bias and ± 0.23 dex dispersion in $\delta \log[O\,III]/H\beta$ for the full sample. This happens because our limits on [O III]/Hα are not as constraining as those for [N II]/Hα (see Fig. 3). Also, [O III] is alone in filter J0515, which makes it prone to be misused to fit positive noise. Again, most of these caveats apply to the weak line regime. As illustrated by the darker histograms in Fig. 7, imposing a $W > 5$ Å cut in [O III] and Hβ eliminates the bias and reduces the scatter to just 0.09 dex. O3N2 is the most uncertain index discussed here. Only when all four lines involved are stronger than 10 Å its scatter approaches 0.1 dex, though it may still be of statistical value for galaxies with weaker lines ELs.

We thus find that relatively reliable line ratios are obtainable with this method, particularly when focusing on sources with strong lines ($W > 5$ Å). This offers the prospect of estimating nebular metallicities

(with either [N II]/Hα or O3N2), as well as EL dust reddening (via Hα/Hβ).

3.5 Degeneracies

Spectral synthesis analysis is notoriously prone to degeneracies between age, dust, and metallicity (see Conroy 2013 and references therein). Because of the disparity in the amount of input information, these degeneracies are more severe for photometric than for full spectral synthesis. The simulations above show that our method is able to recover spectroscopic-based estimates of stellar and EL properties to a good level of accuracy. It is nevertheless useful to inspect degeneracies among our estimated properties, as this has not been done before for S-PLUS and the methodology employed here.

Fig. 8 addresses this issue. The off diagonal panels in this corner plot show how the difference (δ) between our estimate and the W19 one for a given property correlates with the δ in another property. The panels involving $\log M_\star$, $\langle\log t\rangle_L$, $\langle\log Z\rangle_L$, and A_V show well-known degeneracies inherent to stellar population properties. For instance, $\delta\langle\log t\rangle_L$ anticorrelates with both δA_V (the age–dust degeneracy) and $\delta\langle\log Z\rangle_L$ (the age–metallicity degeneracy), reflecting the fact increasing values of any one of these properties leads to a redder spectrum, so that overestimated ages are compensated by underestimated extinction or metallicity. Similarly, the positive correlation between $\delta\langle\log t\rangle_L$ and $\delta\log M_\star$ is due to the well-established fact that older populations have larger mass-to-light ratios.

The main novelty in our methodology is the simultaneous fitting of both stellar and EL properties, an approach that could, in principle, spur new modes of degeneracies. The panels involving $\log W_{\mathrm{H}\alpha}$ and $\log W_{\mathrm{H}\alpha\,\mathrm{N\,II}}$ show that this is *not* the case. Neither $\delta\log W_{\mathrm{H}\alpha}$ nor $\delta\log W_{\mathrm{H}\alpha\,\mathrm{N\,II}}$ correlate with any of the stellar population properties, and the same is true for other ELs. We attribute this to the fact that the EL base spectra, with their ups and downs from one filter to the next (Fig. 2), are completely unlike the stellar spectra, which change more smoothly with λ. This dissimilarity prevents confusion between EL and stellar components, explaining the lack of correlation seen in Fig. 8. We thus conclude that, at least in the empirically motivated way explored in this study, fitting for both stellar EL properties does not lead to significant degeneracies other than those typical of stellar population work.

4 EXAMPLE APPLICATIONS

The performance of ALSTAR in the simulations of the previous section confirmed our basic expectations with respect to the stellar population properties, and exceeded them with respect to ELs. In this section, we present some example applications to actual S-PLUS data. The goal is merely to illustrate the quality of spectral fits obtained and the reasonability of the inferred properties.

For the applications below, a couple of modifications are made with respect to the ALSTAR runs in Section 3. First, the smallest metallicity is 0.2 $Z_\odot$, reducing the base from 7 to 5 Z values. The lowest Z models are very rarely used anyway (see Fig. 4). A second difference is that, for each band, we modify the input photometric errors ϵ_λ by adding (in quadrature) a minimum error to ensure that the S/N does not exceed $S/N_{\max} = 100$. This is equivalent to accounting for an uncertainty in the models, i.e. to acknowledge that the method and its ingredients are not perfect enough to fit perfect data. This affects mostly the MC statistics and only in the limit of high S/N.
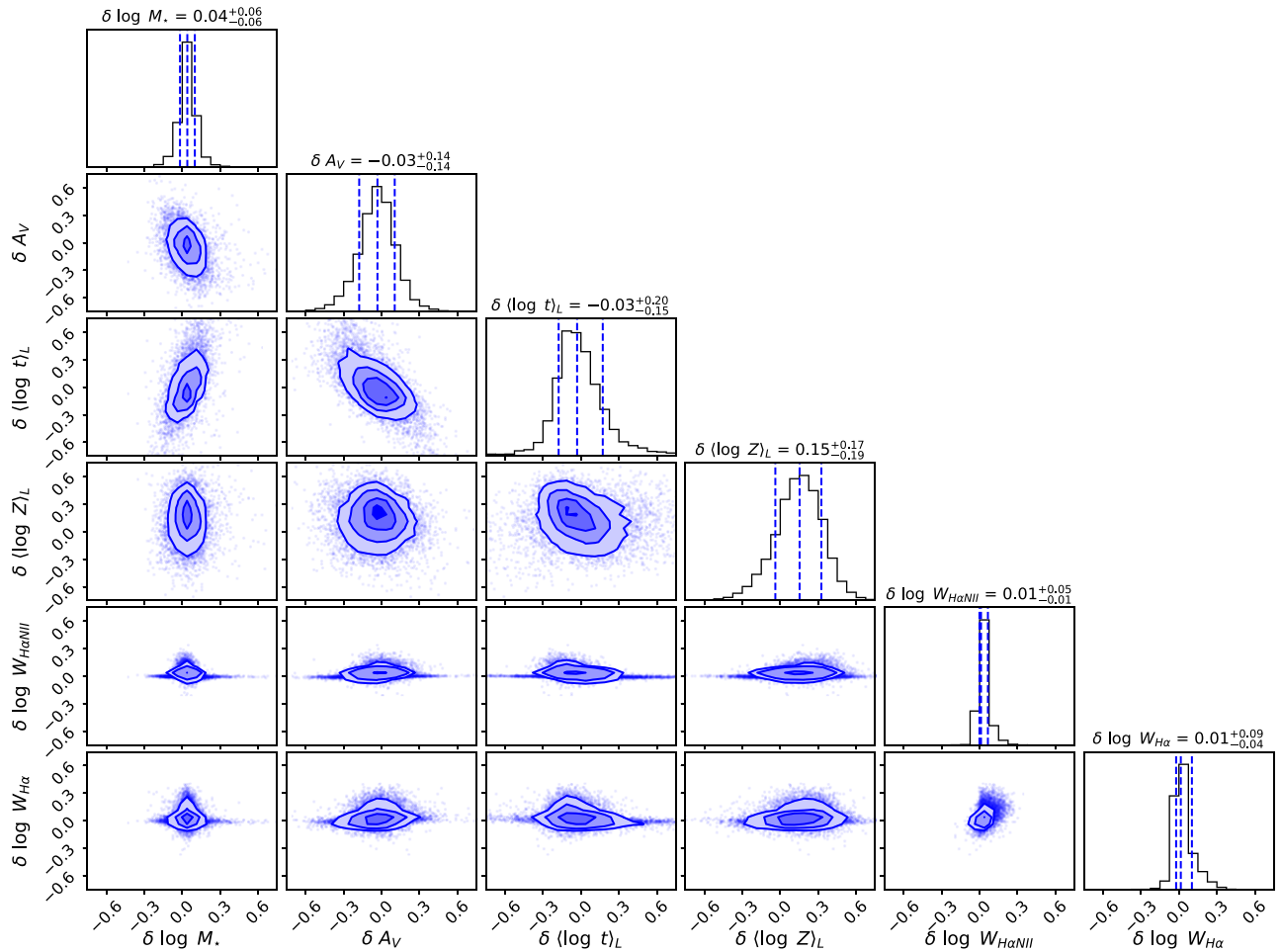
Figure 8. Corner plot (Foreman-Mackey 2016) illustrating the degeneracies between different stellar and EL properties for the $S/N_r = 50$ simulations described in the text. Each panel shows the δ = output − input difference between our estimate of a given property (the output) and that by W19 (the input) against the δ in another property. The four contour levels correspond to 0.5σ, 1σ, 1.5σ, and 2σ equivalent levels. Plots along the diagonal show the histograms of the δs of the property in the *x*-axis, with dashed blue lines marking the 16, 50, and 84 percentiles.

4.1 NGC 1365 and NGC 1379

We have chosen NGC 1379 (an elliptical galaxy) and NGC 1365 (a barred spiral), both in the Fornax Cluster, to illustrate the application of ALSTAR to integrated light S-PLUS data. Details on these and other Fornax integrated photometry, based on the S-PLUS Data Release 4 (DR4; Herpich et al., in preparation), will be presented in a forthcoming paper (Smith Castelli et al., in preparation). The observed photometry is shown in black in Fig. 9, along with the ALSTAR fits (in red) and composite images.

The fits to the photometry are visibly excellent, with a mean absolute deviation between data and model of 1.7 per cent and 2.8 per cent for NGC 1379 and NGC 1365, respectively. Our fits yield $\log M_\star/M_\odot = 10.48$ for NGC 1379 and 10.86 for NGC 1365. These values compare very well with previous estimates. For instance, Iodice et al. (2019a) derived a value of 10.42 for NGC 1379 on the basis of VLT Survey Telescope (VST) photometry and the Taylor et al. (2011) recipe for M/L_i as a function of $g - i$. Similarly, Raj et al. (2019) and Su et al. (2022) estimate $\log M_\star/M_\odot = 10.81$ and 11.00 for NGC 1365.

A detailed comparison with spectroscopy-based stellar and EL properties is complicated by the fact that, because of their proximity, such studies cover only part of the galaxy, whereas the data in Fig. 9 correspond to the whole galaxies. Let us nevertheless make a rough
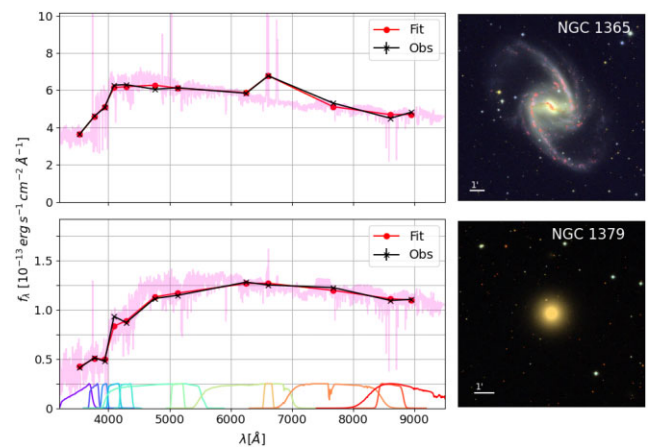

Figure 9. Example ALSTAR fits of S-PLUS data for two galaxies. The data are plotted in black crosses, while the model photometric fluxes are plotted as red circles. The model spectrum is plotted in magenta. The images are composites built with the J0660, *r*, and *g* fluxes for NGC 1365, and *i*, *r*, and *g* for NGC 1379, in the R, G, and B channels, respectively.
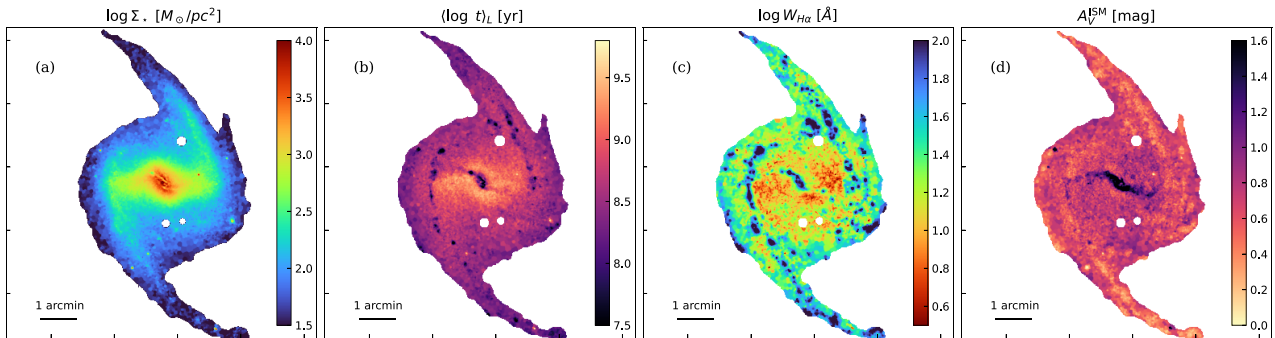
Figure 10. Example of IFS-like science with S-PLUS data for NGC 1365. (a) Stellar mass surface density ($\Sigma_\star$); (b) luminosity-weighted mean log age ($\langle \log t \rangle_L$); (c) Hα equivalent width ($W_{H\alpha}$); and (d) stellar extinction (A_V) maps.
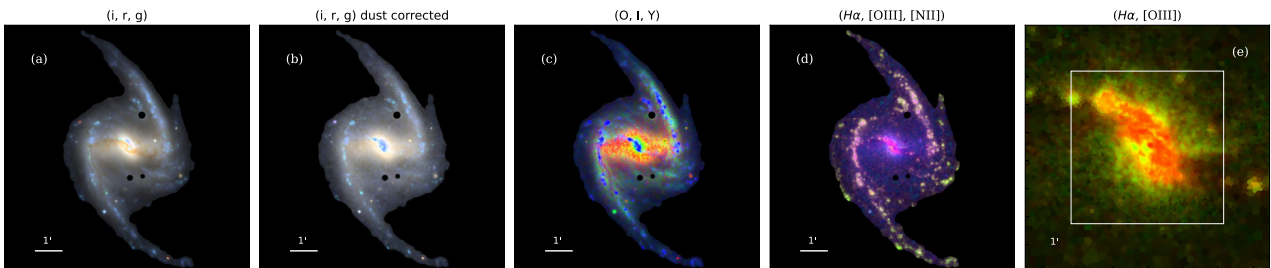

Figure 11. RGB composites combining, respectively, the (a) observed *i*-, *r*-, and *g*-band fluxes; (b) the dust-corrected *i*, *r*, and *g* fluxes; (c) the 5635 Å continuum fluxes associated with old, intermediate, and young populations; and (d) the Hα, [O III], and [N II] fluxes. Panel (e) shows a map of Hα (in R) and [O III] (in G) of the central region, to be compared to the same map produced by Venturi et al. (2018, their fig. 1) on the basis of MUSE data (field of view shown as a box).

comparison with the Multi-Unit Spectroscopic Explorer (MUSE)-based results for NGC 1379 presented in Iodice et al. (2019b). Their stellar population analysis indicates a log age/yr of 10.11 over the inner $0.5R_e$ ($\sim$14.3 arcsec), whereas our whole-galaxy estimate suggests similar ages: $\langle \log t \rangle_L = 10.01$ yr and $\langle \log t \rangle_M = 10.09$ yr. Considering the very different methodologies, very different data, and different apertures, these estimates can be seen as broadly compatible, in the sense that both point to a dominance of old stellar populations. Regarding metallicities, our whole-galaxy estimates are $\langle \log Z/Z_\odot \rangle_L = -0.12$ and $\langle \log Z/Z_\odot \rangle_M = -0.17$, while Iodice et al. (2019b) obtain -0.13 over the central $0.5R_e$.

Regarding ELs, the ALSTAR fits of NGC 1379 yield $W_{H\alpha \, N II} = 5.8$ Å, $W_{H\alpha} = 2.5$ Å, and [N II]/H$\alpha = 0.98$ for the whole galaxy. These values suggest a retired galaxy classification (Cid Fernandes et al. 2011) and are consistent with what would be expected from an early-type galaxy. For NGC 1365 we find integrated EL properties consistent with an SF galaxy, with $W_{H\alpha \, N II} = 40.4$ Å, $W_{H\alpha} = 31.02$ Å, [N II]/H$\alpha = 0.22$, and [O III]/H$\beta = 0.79$. As with NGC 1379, previous spectroscopic work on this galaxy focuses on its inner regions, hindering a proper comparison with these galaxy-wide estimates.

These two examples fulfil the goal of illustrating the performance of ALSTAR with real S-PLUS integrated-light data. Let us now examine the potential of S-PLUS + ALSTAR for spatially resolved work.

4.2 Data cubes

For nearby galaxies we can perform a spatially resolved analysis similar to that obtained with integral field spectroscopy (IFS). The two galaxies examined in integrated light in the previous section are examples of cases where a spatial analysis is clearly warranted.

As a first experiment of IFS-like work with S-PLUS, let us examine the ALSTAR maps obtained for NGC 1365. The cube comprises 1100×1100 pixels (10.08×10.08 arcmin^2). Besides a basic S/N spatial mask, we have further applied a low-pass (Butterworth) filter and Voronoi binning (to reach a target S/N of 20 in the five bluest filters combined). Details on these pre-processing steps will be presented elsewhere. The same stellar base described in the previous section was used. Also, the EL base and constraints are the same ones discussed in Section 2.3.

Fig. 10 illustrates the results. ALSTAR-based maps of the stellar mass surface density ($\Sigma_\star$), $\langle \log t \rangle_L$, $W_{H\alpha}$, and A_V^{ISM} are shown in panels (a)–(d), respectively. The spatial correspondence between regions of low age and large $W_{H\alpha}$ (and vice versa) is evident to the eye, illustrating that, without being forced to do so (which would be an acceptable strategy), the code identifies H II regions both in the stellar and nebular components. The dust lane across the bar and nucleus is neatly visible in panel (d). The age and dust maps indicate that star formation is plentiful in the central region, but not along the larger scale bar in which it is embedded.

Fig. 11 shows some other products of our S-PLUS + ALSTAR analysis. Panel (a) shows an RGB composite based on the observed *i*, *r*, and *g* S-PLUS fluxes. Panel (b) shows the same composite, but after correcting the fluxes by dust attenuation. Visibly, the bar-aligned dust lane disappears in the dedusted image. Panel (c) shows the continuum fluxes (at our normalization wavelength of 5635 Å) associated with old ($t > 1$ Gyr), intermediate (10 Myr–1 Gyr), and young (≤ 10 Myr) stellar populations, colour coded onto R, G, and B channels, respectively. This higher order version of the $\langle \log t \rangle_L$ map in Fig. 10 reveals a mixture of young and intermediate age populations in the central parts, the young stars in the spiral arms, and the predominantly old ones along the bar.
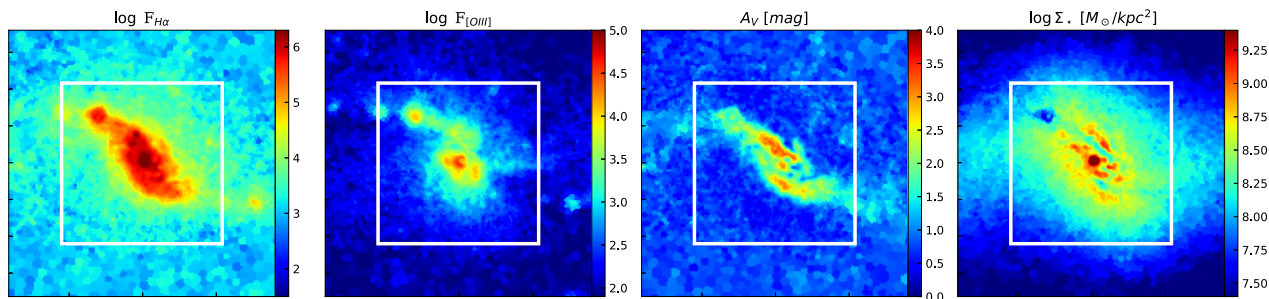
Figure 12. Zoom on the inner maps of $F_{H\alpha}$, $F_{[O\,III]}$ (both in units of 10^{-20} erg s^{-1} cm^{-2}, adjusted by the pixel scale difference between MUSE and S-PLUS), A_V, and $\Sigma_\star$. The colour scales are matched to those of the same images in the Gao et al. (2021), who produced maps of these quantities derived on the basis of MUSE data over the inner $\sim 1 \times 1$ arcmin^2 (marked by a box). The A_V map shown corresponds to the extinction applied to young stars and ELs (i.e. the sum of ISM and BC components), as this is more comparable to the Hα/Hβ-based A_V map of Gao et al. (2021).

Fig. 11(d) shows an Hα (in the R channel), [O III] (G channel), and [N II] (B channel) composite. Hα dominates the emission in the central regions. This reflects both the SF activity in this region and the high dust content, which attenuates the [O III] emission. H II regions along the spiral arms also stand out clearly. The greener (stronger [O III]) colours of the outer H II regions in this image are indicative of a negative nebular metallicity gradient, qualitatively consistent with what one expects for disc galaxies in general and for NGC 1365 in particular (Chen et al. 2023). The fainter emission (e.g. between the nucleus and the arms) has both lower $W_{H\alpha}$ (panel c in Fig. 10) and larger [N II]/Hα (of order 0.5), consistent with the properties of diffuse ionized gas in spirals (e.g. Lacerda et al. 2018; Vale Asari et al. 2019).

The rightmost panel in Fig. 11 shows Hα (in the R channel) and [O III] (G channel) fluxes in the inner region of NGC 1365. This figure was made with the explicit goal of comparing it with the same map obtained from MUSE data by Venturi et al. (2018). The image reveals both the circumnuclear star formation, bright in Hα, and the [O III]-bright biconical outflow originating from the Seyfert nucleus of this galaxy. Despite the huge differences in collecting aperture, exposure time, and spectral resolution, the S-PLUS + ALSTAR map in Fig. 11(e) looks like a coarser version of fig. 1(d) of Venturi et al. (2018), again illustrating the power of S-PLUS as an IFS-like machine for nearby galaxies.

This potential is further illustrated in Fig. 12, where we zoom in on the inner ~ 1 arcmin maps of the (from left to right) Hα and [O III] fluxes, A_V, and $\Sigma_\star$ maps. These same properties were estimated on the basis of a full spectral analysis of MUSE data by Gao et al. (2021). Comparing our results with theirs reveals a very good level of agreement, especially considering the differences in resolution. The knot at the top-left of the MUSE box in Fig. 12 corresponds to cluster ID 37 of the Whitmore et al. (2023) study, which reports a log age/yr of 6.5 (6.6) and A_V of 2.0 (2.6) mag with the *Hubble Space Telescope − HST* (*JWST*) data. These values compare well with our $\langle \log t \rangle_L = 6.87$ and $A_V = 2.67$ mag. These examples show that S-PLUS is capable of producing useful estimates of spatially resolved properties of both stellar population and ELs in the local Universe.

To close, let us compare our ALSTAR-based estimates of the total Hα + [N II]6548, 6584 flux ($F_{H\alpha\,N\,II}$) with those based on the cruder, but more direct estimates obtained with the so-called three-filter method (3FM; Vilella-Rojo et al. 2015).[6] Fig. 13 compares the $F_{H\alpha\,N\,II}$ values obtained with the two methods for Voronoi zones in NGC 1365
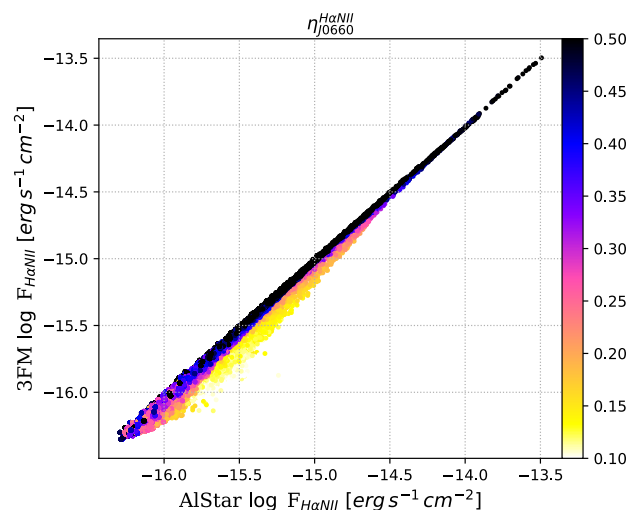

Figure 13. Comparison of the [N II]6548 + Hα + [N II]6584 fluxes obtained by the three-filter method (3FM; *r*, J0660, and *i*) and those from our analysis for 4431 Voronoi zones in NGC 1365. Points are colour coded by fraction of the total J0660 flux that is due to these ELs.

(see Lopes et al., in preparation, for more examples). The comparison is limited to the 4431 zones where the 3FM estimate of $F_{H\alpha\,N\,II}$ exceeds its uncertainty (i.e. S/N > 1). Points are coloured by the fraction $\eta_{J0660}^{H\alpha\,N\,II}$ of the total J0660 flux that comes from these three lines.

The plot shows that the ALSTAR and 3FM estimates agree very well, with a median $\pm \sigma_{NMAD}$ of the $\delta =$ ALSTAR minus 3FM values of $\delta \log F_{H\alpha\,N\,II} = 0.068 \pm 0.061$ dex. As seen in Fig. 13, the agreement is even better when ELs contribute more to the J0660 flux. For instance, we find $\delta \log F_{H\alpha\,N\,II} = 0.032 \pm 0.021$ dex for zones where $\eta_{J0660}^{H\alpha\,N\,II} > 30$ per cent. The difference for zones with small $\eta_{J0660}^{H\alpha\,N\,II}$ is partly due to the effect of the Hα absorption component (included in ALSTAR but not in the 3FM), which explains the somewhat larger values obtained by ALSTAR.

---

[6]Our implementation of this method includes the effects of [N II]$\lambda\lambda$6548, 6584, Hα, and [S II]$\lambda\lambda$6717, 6731 lines on the *r*, J0660, and

i bands. It is thus somewhat more elaborate than that used in Vilella-Rojo et al. (2015), though, in practice, the two approaches yield very similar results.

5 SUMMARY

S-PLUS is currently building a huge data set of galaxy photometry in its seven narrow and five broad bands system. Transforming these 12 fluxes onto astrophysical information on stellar population and EL properties requires tools such as the ALSTAR code tested in this study.

After reviewing ALSTAR basics and introducing a novel semi-empirical strategy to improve its EL estimation power (Section 2), we have applied the code to synthetic photometry of ∼10 000 SDSS galaxies (Section 3), shifted to $z = 0.01$ to ensure the main optical ELs are sampled in S-PLUS narrow bands. Noise with a spectrum characteristic of S-PLUS was added to these data to achieve r-band S/N typical of the envisaged near-Universe applications. The output stellar population and EL properties of these runs were then compared to those obtained by a previous detailed λ-by-λ full spectral analysis (W19). The results of these comparisons may be summarized as follows.

(i) Stellar population properties recovered from the 12 S-PLUS bands compare well with those obtained from full spectral fitting. The statistics (median $\pm \sigma_{\mathrm{NMAD}}$) of $\delta =$ output − input differences are $\delta \log M_\star = 0.04 \pm 0.06$ dex, $\delta \langle \log t \rangle_L = -0.03 \pm 0.16$ dex, $\delta \langle \log Z \rangle_L = 0.15 \pm 0.18$ dex, and $\delta A_V = -0.03 \pm 0.14$ mag for S/N$_r =$ 50. Even for the lowest S/N$_r$ in our simulations we find acceptable differences given the huge compression in the observational input in going from a full spectrum to its 12-bands S-PLUS representation. We conclude that S-PLUS is able to provide a useful first-order characterization of stellar population properties even at relatively low S/N$_r$.

(ii) The main focus of this work was on ELs. We model their contribution to the S-PLUS photometry by complementing the stellar base with an EL base built to mimic ELs as found in real galaxies. Stellar and EL components are fitted simultaneously. The specific EL base used in this work was built on the basis of the BPT diagram of SDSS galaxies. This scheme guarantees that the output EL properties are realistic (though not necessarily accurate).

(iii) Confirming previous J-PLUS work, because they all fall under the J0660 filter, the sum of Hα and [N II]6548, 6584 fluxes is always well recovered. Quantitatively, we retrieve their combined equivalent width ($W_{\mathrm{H}\alpha\,\mathrm{N\,II}}$) to within ±0.02 dex for our test sample, which (by design) spans from weak ($W_{\mathrm{H}\alpha} = 1$ Å) to strong (>100 Å) EL systems.

(iv) The novelty comes in our ability to disentangle Hα from [N II], as well as to estimate other ELs with remarkable precision for a photometric survey. This is achieved by imposing priors on the EL base guided by an initial (but robust) estimate of the value of $W_{\mathrm{H}\alpha\,\mathrm{N\,II}}$. We use SDSS data to calibrate $W_{\mathrm{H}\alpha\,\mathrm{N\,II}}$-based constraints on the [N II]/Hα and [O III]/Hβ ratios that, despite a few caveats, greatly improve our ability to recover EL properties beyond Hα + [N II].

(v) For the full 10 000 sample and S/N$_r = 50$ we obtain $\delta = \log W$ is 0.04 ± 0.16, 0.04 ± 0.08, 0.13 ± 0.23, 0.01 ± 0.05, 0.01 ± 0.08, and 0.03 ± 0.13 dex for [O II], Hβ, [O III], Hα, [N II], and [S II], respectively. These statistics, which are already remarkably good, get even better for lines detected with $W > 5$ Å.

We have further presented example applications of the code to real S-PLUS data, including integrated light photospectra and a data cube (Section 4). This second part of the paper showed the following.

(i) The method is capable of producing excellent fits to S-PLUS data. For the two whole galaxy examples shown, the model matches the data to within 2.8 per cent (NGC 1365) and 1.7 per cent (NGC 1379). The derived stellar masses agree well with those

obtained from independent photometry and a different method. Because of their large angular extents, spectroscopic estimates of the stellar and EL properties of these two galaxies are available only for their central regions. Considering this caveat, as well as the differences in methodology and definitions, our rough comparison with literature results showed a reasonable level of agreement.

(ii) One of the main applications envisaged for the method developed here is to obtain spatially resolved maps of stellar population and EL of nearby galaxies. A ∼10 × 10 arcmin^2 data cube for NGC 1365 was analysed to showcase this kind of application. The resulting maps trace very well the main stellar, dust, and EL structures across this barred spiral. Comparison with previous MUSE-based properties derived for the inner regions reveals a very good level of agreement, reinforcing the potential of S-PLUS + ALSTAR for IFS-like work.

Next steps include work both on the data and methodological fronts. Including more bands in the analysis [say, the *GALEX* near-ultraviolet (NUV) and far-ultraviolet (FUV) filters], for instance, is straightforward. Similarly, application to J-PAS photometry would both lead to better constraints and extend the redshift range of applicability. Regarding the method itself, a promising way forward is to generalize the $W_{\mathrm{H}\alpha\,\mathrm{N\,II}}$-based empirical prior used to improve the EL estimation. Given the plethora of correlations between observed properties of galaxies (e.g. Worthey & Ottaviani 1997; Kennicutt 1998; Tremonti et al. 2004; Quilley & de Lapparent 2022), one can envisage a more informative prior including, for instance, data on morphology or colours, to further improve the estimation of EL properties out of photometric surveys like S-PLUS.

DATA AVAILABILITY

The complete S-PLUS DR4 catalogues and reduced fits images are available in the S-PLUS Cloud Database at https://splus.cloud. The catalogues can also be accessed in TOPCAT using the TAP URL: https://splus.cloud/public-TAP/tap, and through the PYTHON package SPLUSDATA (see documentation and source code at https://github.com/Schwarzam/splusdata). The code with which the cubes were produced is available at https://github.com/splus-collab/splus-cubes.

REFERENCES

Almeida-Fernandes F. et al., 2022, MNRAS, 511, 4590
Asari N. V., Cid Fernandes R., Stasińska G., Torres-Papaqui J. P., Mateus A., Sodré L., Schoenell W., Gomes J. M., 2007, MNRAS, 381, 263
Baldwin J. A., Phillips M. M., Terlevich R., 1981, PASP, 93, 5
Barbosa C. E. et al., 2020, ApJS, 247, 46
Bell E. F., McIntosh D. H., Katz N., Weinberg M. D., 2003, ApJS, 149, 289
Bonoli S. et al., 2021, A&A, 653, A31
Bruzual G., 1983, ApJ, 273, 105
Bruzual G., Charlot S., 2003, MNRAS, 344, 1000
Bundy K. et al., 2015, ApJ, 798, 7
Calzetti D., 2001, PASP, 113, 1449
Calzetti D., Armus L., Bohlin R. C., Kinney A. L., Koornneef J., Storchi-Bergmann T., 2000, ApJ, 533, 682
Calzetti D., Kinney A. L., Storchi-Bergmann T., 1994, ApJ, 429, 582
Carnall A. C., Leja J., Johnson B. D., McLure R. J., Dunlop J. S., Conroy C., 2019, ApJ, 873, 44
Carnall A. C., McLure R. J., Dunlop J. S., Davé R., 2018, MNRAS, 480, 4379
Cenarro A. J. et al., 2019, A&A, 622, A176
Chabrier G., 2003, PASP, 115, 763
Charlot S., Fall S. M., 2000, ApJ, 539, 718
Chen Q.-H., Grasha K., Battisti A. J., Kewley L. J., Madore B. F., Seibert M., Rich J. A., Beaton R. L., 2023, MNRAS, 519, 4801
Chevallard J., Charlot S., 2016, MNRAS, 462, 1415
Cid Fernandes R., Gu Q., Melnick J., Terlevich E., Terlevich R., Kunth D., Rodrigues Lacerda R., Joguet B., 2004, MNRAS, 355, 273
Cid Fernandes R., Mateus A., Sodré L., Stasińska G., Gomes J. M., 2005, MNRAS, 358, 363
Cid Fernandes R., Stasińska G., Mateus A., Vale Asari N., 2011, MNRAS, 413, 1687
Cid Fernandes R., Stasińska G., Schlickmann M. S., Mateus A., Vale Asari N., Schoenell W., Sodré L., 2010, MNRAS, 403, 1036
Conroy C., 2013, ARA&A, 51, 393
da Cunha E., Charlot S., Elbaz D., 2008, MNRAS, 388, 1595
Dopita M. A., Sutherland R. S., 2003, Astrophysics of the Diffuse Universe. Springer-Verlag, Berlin
Foreman-Mackey D., 2016, J. Open Source Softw., 1, 24
Gao Y., Egusa F., Liu G., Kohno K., Bao M., Morokuma-Matsui K., Kong X., Chen X., 2021, ApJ, 913, 139
González Delgado R. M. et al., 2021, A&A, 649, A79(GD21)
Heavens A., Panter B., Jimenez R., Dunlop J., 2004, Nature, 428, 625
Iodice E. et al., 2019a, A&A, 623, A1
Iodice E. et al., 2019b, A&A, 627, A136
Kauffmann G. et al., 2003, MNRAS, 341, 33
Kennicutt R. C. J., 1998, ApJ, 498, 541
Lacerda E. A. D. et al., 2018, MNRAS, 474, 3727
Leja J., Carnall A. C., Johnson B. D., Conroy C., Speagle J. S., 2019, ApJ, 876, 3
Lima E. et al., 2022, Astron. Comput., 38, 100510
Lima-Dias C. et al., 2021, MNRAS, 500, 1323
Logroño-García R. et al., 2019, A&A, 622, A180
Lumbreras-Calle A. et al., 2022, A&A, A60, 0004
Mendes de Oliveira C. et al., 2019, MNRAS, 489, 241
Molino A. et al., 2020, MNRAS, 499, 3884
Nakazono L. et al., 2021, MNRAS, 507, 5847
Noll S., Burgarella D., Giovannoli E., Buat V., Marcillac D., Muñoz-Mateos J. C., 2009, A&A, 507, 1793
Pettini M., Pagel B. E. J., 2004, MNRAS, 348, L59
Placco V. M. et al., 2021, ApJ, 912, L32
Quilley L., de Lapparent V., 2022, A&A, 666, A170
Raj M. A. et al., 2019, A&A, 628, A4
Riffel R., Pastoriza M. G., Rodríguez-Ardila A., Bonatto C., 2009, MNRAS, 400, 273
Rola C., Pelat D., 1994, A&A, 287, 676
Sánchez S. F. et al., 2016, A&A, 594, A36
Sánchez S. F. et al., 2022, ApJS, 262, 36
Stasińska G., Asari N. V., Cid Fernandes R., Gomes J. M., Schlickmann M., Mateus A., Schoenell W., Sodré L., Jr, 2008, MNRAS, 391, L29
Su A. H., Salo H., Janz J., Venhola A., Peletier R. F., 2022, A&A, 664, A167
Taylor E. N. et al., 2011, MNRAS, 418, 1587
Tremonti C. A. et al., 2004, ApJ, 613, 898
Vale Asari N., Couto G. S., Cid Fernandes R., Stasińska G., de Amorim A. L., Ruschel-Dutra D., Werle A., Florido T. Z., 2019, MNRAS, 489, 4721
Venturi G. et al., 2018, A&A, 619, A74
Vidal-García A., Charlot S., Bruzual G., Hubeny I., 2017, MNRAS, 470, 3532
Vilella-Rojo G. et al., 2015, A&A, 580, A47
Walcher J., Groves B., Budavári T., Dale D., 2011, Ap&SS, 331, 1
Werle A., Cid Fernandes R., Vale Asari N., Bruzual G., Charlot S., Gonzalez Delgado R., Herpich F. R., 2019, MNRAS, 483, 2382(W19)
Wesson R., Stock D. J., Scicluna P., 2016, MNRAS, 459, 3475
Whitmore B. C. et al., 2023, ApJ, 944, L14
Whitten D. D. et al., 2021, ApJ, 912, 147
Worthey G., Ottaviani D. L., 1997, ApJS, 111, 377

This paper has been typeset from a TeX/LaTeX file prepared by the author.